IET Electrical Systems in Transportation

Special Issue: Selected Papers from the 2017 and 2018 IEEE Vehicle Power and Propulsion Conference

IET Journals
The Institution of Engineering and Technology

Design of flux-weakening space vector control algorithms for permanent magnet brushless DC machines on suitable synchronous reference frames

ISSN 2042-9738
Received on 28th February 2019
Revised 31st July 2019
Accepted on 22nd August 2019
E-First on 4th December 2019
doi: 10.1049/iet-est.2018.5108
www.ietdl.org

Alessandro Serpi[1,2] ✉, Mario Porru[1,2], Giuseppe Fois[1,2], Alfonso Damiano[1]

[1]*Department of Electrical and Electronic Engineering, University of Cagliari, Via Marengo 2, Cagliari, Italy*

[2]*Novel Electric Propulsion Systems, NEPSY srl, Via Logudoro 8, Cagliari, Italy*

✉ *E-mail: alessandro.serpi@diee.unica.it*

Abstract: The design of space vector control (SVC) systems suitable for flux-weakening operation of permanent magnet brushless DC machines (PMBDCMs) is presented in this study. The proposed design approach enables overcoming the critical issues arising from the non-linearities of PMBDCM voltage and torque equations; these issues derive from the trapezoidal shapes of back-emfs and affect PMBDCM constraint management significantly. The SVCs presented in this study have been developed within two different synchronous reference frames, both of which enable distinguishing torque and demagnetising current components clearly. Therefore, reference torque current component is determined in accordance with PMBDCM torque demand, while reference demagnetising current component is computed through a voltage follower PI regulator, which processes the voltage deficit detected on the DC-link. In this regard, a novel synchronous reference frame is proposed in this study, which improves PMBDCM constraint management and results into a wider constant-power speed range, but at the cost of some torque ripple. The enhanced performances achievable by SVC approaches are highlighted by numerical simulations, which regard the comparison among the SVCs and an SVC with no flux-weakening capability, at different operating conditions.

Nomenclature

u,v,w	phases of stator winding
x, y, z	incoming, non-commutating and outcoming phases
σ	sign variable
%, $^-$	mod operator, conjugate operator
$\alpha\beta$	stationary reference frame
dq	synchronous reference frame
ft, $\varphi\tau$	novel synchronous reference frames
γ, δ	transformation vectors ($\alpha\beta$–ft)
$\tilde{\gamma}$, $\tilde{\delta}$	transformation vectors ($\alpha\beta$–$\varphi\tau$)
x_n	rated value of x
$\underline{x}$, $\hat{x}$	average value of x, maximum/peak value of x
v, $\tilde{v}$	voltage and auxiliary voltage vectors
i, e	current and back-emf vectors
I, E	current and back-emf magnitudes
r	phase resistance
L	synchronous inductance
p	number of pole pairs
Λ	equivalent flux linkage due to PMs
ϑ, ω	electric rotor position, electric rotor speed
ϑ_m, ω_m	rotor position, rotor speed
ϑ_{pu}, ω_{pu}	per-unit rotor position and speed
T_e, P_m	electromagnetic torque and power
$\psi_{\varphi\tau}$	torque corrective factor
V_{DC}	DC-link voltage
ξ	L-based emf vector
$\mathscr{C}_{TP}$	T_e and P_m limitation constraint
$\mathscr{C}_i$	current limitation constraint
$\mathscr{C}_V$	voltage saturation constraint
ς, ρ	centre and radius of $\mathscr{C}_V$

1 Introduction

Permanent magnet brushless DC machines (PMBDCMs) have been usually considered for low-performance applications mostly [1]; in this regard, they are quite cheap to manufacture and simple to control, especially as far as the well-known current commutation control is concerned. Consequently, large PMBDCM torque ripple has been widely and usually accepted because high-performance applications have relied on vector-controlled permanent magnet brushless AC machines (PMBACMs). However, PMBDCMs show great potentialities, especially in terms of higher torque density and reduced Joule losses compared to PMBACMs [2, 3]. Therefore, PMBDCM may be suitable also for high-performance applications, such as distributed power generation and electric propulsion systems [4–8], but on condition that advanced control algorithms are employed; this is not the case of conventional current commutation controls, which are characterised by high torque ripple and narrow speed range.

In the context of PMBDCM advanced management and control strategies, a number of different control approaches have been proposed [9–30]. Some of these focus on improving conventional current commutation control [15–20], e.g. by carrying out current commutation in advance [17, 18] or by varying DC-link voltage suitably [19, 20]. The application of direct torque control has been also investigated [21, 22], together with various vector control systems [23–30]. Most of these research efforts have been focused on suppressing or reducing PMBDCM torque ripple due to current commutation, but enhancing PMBDCM flux-weakening capability has been sometimes also consider [16–18, 23, 29]. In this regard, the space vector control (SVC) presented in [25] is based on a novel ft reference frame, which enables identifying torque and demagnetising current components clearly. Consequently, PMBDCM torque and flux-weakening operation needs can be satisfied simultaneously, resulting in enhanced performances compared to conventional current commutation control approaches [25]. However, the SVC proposed in [25] does not exploit any flux-weakening capability because the demagnetising current component is held constant at zero at any PMBDCM operating condition.

In the view of developing a flux-weakening control strategy suitable for PMBDCM, reference can be made to the several flux-weakening approaches proposed in the literature, which can be classified as pure electric or design-based methods [31]. The

former consists in injecting a demagnetising current at high speed operation, even by means of auxiliary DC windings. Pure electric methods can be split further into feed-back, feed-forward and combined approaches [32, 33]. Feed-back methods [34–38] are quite robust against parameter variations and uncertainties at the cost of limited dynamic performances; this is because they synthesise the reference demagnetising current through a PI regulator, which can be alternatively fed by voltage or current errors. Enhanced dynamic performances are instead guaranteed by feed-forward approaches [39–44], which rely on appropriate look-up tables and/or predictive control systems. However, increased dynamic performances come at the cost of high sensitivity to parameter variations and uncertainties. Combined methods [44, 45] attempt to incorporate the advantages of both feed-back and feed-forward methods by employing advanced but more complex control algorithms.

Among the several flux-weakening approaches above-mentioned, feed-back methods seem the most appropriate for PMBDCM as they should not suffer from modelling simplifications excessively; the latter are required by the non-linearities characterising the PMBDCM voltage equation, even in the ft synchronous reference frame [25]. Therefore, a demagnetising current loop has been designed in [46] by means of a voltage follower PI regulator [34]; the latter processes the voltage deficit detected on the DC-link at the aim of determining the most suitable reference demagnetising current profile beyond the rated speed. Hence, in [46], a flux-weakening SVC (FW-SVC) is applied for driving the high-speed PMBDCM designed in [47], in comparison with a conventional current commutation control and with the SVC already proposed in [25]. However, although the FW-SVC proposed in [46] shows improved performances compared to the other two PMBDCM control approaches in terms of both constant-power speed range (CPSR) and maximum speed, the latter are still quite far from the targets foreseen in [47]. In particular, a CPSR of about 3.3 and a maximum speed of 100 krpm are expected, whereas those achieved by the FW-SVC proposed in [46] are about 1.75 and 57 krpm, respectively. If maximum speed could be increased by lightening the load torque appropriately, the same does not go for CPSR, which cannot be expected to increase significantly. As a result, still unsatisfactory PMBDCM performances have been achieved, even resorting to an advanced FW-SVC system.

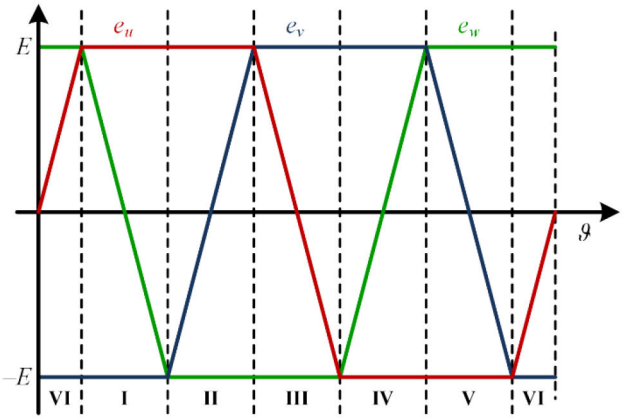

Fig. 1 *Evolutions of the PMBDCM back-emfs (e_u, e_v and e_w) with the electrical rotor position (ϑ), together with the corresponding operating sectors (I–VI)*

In this context, an alternative FW-SVC is proposed in this paper at the aim of extending both CPSR and maximum speed of PMBDCM. In particular, a novel φτ reference frame is defined in order to achieve a more effective PMBDCM constraint management, especially in terms of voltage saturation. This goal is achieved at the cost of some torque ripple, which is instead prevented by using the FW-SVC proposed in [46]. For this reason, a detailed analysis of both these FW-SVCs is presented in this paper, by highlighting their most important advantages and drawbacks. Subsequently, PMBDCM performance assessment is carried out through a simulation study, whose results are presented and discussed extensively. In particular, simulations refer to the high-speed PMBDCM designed in [47], which is driven by SVC and by both the FW-SVCs alternatively for comparison purposes.

The paper is structured as follows: PMBDCM mathematical modelling is presented in Section 2; the ft and the novel φτ synchronous reference frames are presented in Section 3, together with the corresponding PMBDCM operating constraint analyses; PMBDCM control system design is resumed briefly in Section 4; simulation results are presented and discussed extensively in Section 5; concluding remarks are given in Section 6.

2 PMBDCM mathematical modelling

Considering the ideal back-emf evolutions of a three-phase PMBDCM shown in Fig. 1, the discontinuities occurring on the variation of each back-emf profile prevent the setup of a PMBDCM mathematical model within the overall electrical period. Consequently, the latter should be split into six different sectors (I–VI), within which just one back-emf varies linearly with ϑ, while the others two are constant at maximum and minimum values. Hence, by referring to a generic operating sector, incoming (x), non-commutating (y) and outcoming (z) phases can be distinguished clearly; particularly, $\{x, y, z\}$ denote the phases whose back-emf stops varying (x), does not vary (y) and starts varying (z), as pointed out in Table 1 [10]. This table also accounts for a proper sign variable (σ), which is positive and negative within odd and even sectors, respectively. Hence, assuming a floating neutral point of the PMBDCM star-connected winding, voltage equation can be expressed as

$$\boldsymbol{v} = r\boldsymbol{i} + L\frac{\mathrm{d}\boldsymbol{i}}{\mathrm{d}t} + \boldsymbol{e} \tag{1}$$

where r and L are the phase resistance and the synchronous inductance, respectively, while $\boldsymbol{v}$ and $\boldsymbol{i}$ are the phase voltage and current vectors, respectively,

$$\boldsymbol{v} = \begin{bmatrix} v_x \\ v_y \\ v_z \end{bmatrix}, \quad \boldsymbol{i} = \begin{bmatrix} i_x \\ i_y \\ i_z \end{bmatrix}. \tag{2}$$

Table 1 PMBDCM operating sectors

Sector	Electrical rotor position range	Three-phase terminals			σ
		u	v	w	
I	$\frac{1}{6}\pi \le \vartheta < \frac{1}{2}\pi$	x	y	z	+1
II	$\frac{1}{2}\pi \le \vartheta < \frac{5}{6}\pi$	y	z	x	−1
III	$\frac{5}{6}\pi \le \vartheta < \frac{7}{6}\pi$	z	x	y	+1
IV	$\frac{7}{6}\pi \le \vartheta < \frac{3}{2}\pi$	x	y	z	−1
V	$\frac{3}{2}\pi \le \vartheta < \frac{11}{6}\pi$	y	z	x	+1
VI	$\frac{11}{6}\pi \le \vartheta,\ \vartheta < \frac{1}{6}\pi$	z	x	y	−1

Regarding $\boldsymbol{e}$ appearing in (1), it represents the back-emf vector due to permanent magnets and it can be expressed as

$$\boldsymbol{e} = \sigma E \begin{bmatrix} 1 \\ -1 \\ 1 - 2\vartheta_{\mathrm{pu}} \end{bmatrix}, \quad E = p\omega_m \Lambda \tag{3}$$

in which E is the back-emf magnitude that depends on rotor speed (ω_m), number of pole pairs (p) and on flux linkage due to permanent magnets only (Λ). In addition, ϑ_{pu} is a suitable per-unit position variable that can be computed in accordance with the following relationship:

$$\vartheta_{\mathrm{pu}} = \left(\frac{3}{\pi}\vartheta - \frac{1}{2}\right)\%1, \quad \vartheta_{\mathrm{pu}} \in [0, 1) \tag{4}$$

where % denotes the mod operator that provides just the fractional part of the division by one.

As far as SVC systems are to be developed, (1) can be expressed in terms of voltage and current space vectors in the $\alpha\beta$ stationary reference frame by applying the well-known Clarke transformation, leading to

$$v_{\alpha\beta} = r i_{\alpha\beta} + L\frac{\mathrm{d}i_{\alpha\beta}}{\mathrm{d}t} + e_{\alpha\beta}\,. \tag{5}$$

Therefore, the electromagnetic torque can be determined as

$$T_e = \frac{3}{2}\frac{1}{\omega_m}\Re\left\{e_{\alpha\beta}\cdot \bar{i}_{\alpha\beta}\right\}. \tag{6}$$

Based on (3), $e_{\alpha\beta}$ appearing in both (5) and (6) is

$$e_{\alpha\beta} = j\frac{4}{3}E\left(1 - \vartheta_{\mathrm{pu}} + \vartheta_{\mathrm{pu}}^2\right)\cdot\gamma \tag{7}$$

where

$$\gamma = -\frac{\sigma}{2}\frac{1}{1 - \vartheta_{\mathrm{pu}} + \vartheta_{\mathrm{pu}}^2}\left(\sqrt{3}\left(1 - \vartheta_{\mathrm{pu}}\right) + j\left(1 + \vartheta_{\mathrm{pu}}\right)\right). \tag{8}$$

Therefore, substituting (7) and (3) into (6) yields

$$T_e = 2p\Lambda\left(1 - \vartheta_{\mathrm{pu}} + \vartheta_{\mathrm{pu}}^2\right)\cdot\Im\left\{\bar{\gamma}\cdot\boldsymbol{i}_{\alpha\beta}\right\}. \tag{9}$$

The development of suitable PMBDCM flux-weakening control strategies requires that reference torque (T_e^*) and current vector ($\boldsymbol{i}_{\alpha\beta}^*$) must comply with all PMBDCM operating constraints. In particular, (T_e^*) is constrained by both electromagnetic torque and power limitations, respectively, as

$$|T_e^*| \le T_{e,n}, \quad |T_e^*\cdot\omega_m| \le T_{e,n}\cdot\omega_{m,n} \tag{10}$$

in which rated values are denoted by the subscript 'n'. Furthermore, $\boldsymbol{i}_{\alpha\beta}^*$ must comply with both current limitation and voltage saturation; the former constraint consists of limiting the average magnitude of the current vector in each PMBDCM operating sector. Therefore, denoting by $\hat{I}$ the maximum current allowed over conventional current commutation controls, the following relationships hold:

$$\underline{\left|i_{\alpha\beta}^*\right|^2} \le \frac{4}{3}\cdot\hat{I}^2, \quad \underline{\left|i_{\alpha\beta}^*\right|^2} = \int_0^1 \left|i_{\alpha\beta}^*\right|^2 \mathrm{d}\vartheta_{\mathrm{pu}} \tag{11}$$

in which the operator '$\underline{\ }$' provides the average value within each operating sector, as highlighted in (11). Regarding voltage saturation, it generally consists of limiting the magnitude of the voltage vector in accordance with the following relationship:

$$\left|v_{\alpha\beta}\right| \le \frac{V_{\mathrm{DC}}}{\sqrt{3}} \tag{12}$$

in which V_{DC} is the DC-link voltage. Therefore, starting from (5) and (9), it is possible to develop suitable PMBDCM current control strategies that enable flux-weakening operation by complying with (10)–(12) simultaneously, as detailed in the following section.

3 PMBDCM synchronous reference frames

Considering (5), (7) and (9), it is reasonable to state that the $\alpha\beta$ stationary reference frame is not suitable for developing an effective space vector control for PMBDCM; this is due to the fact that both $e_{\alpha\beta}$ and T_e depend on ϑ_{pu}, which varies significantly within each operating sector. Consequently, the management of PMBDCM operating constraints and the design of any current control loop in the $\alpha\beta$ stationary reference frame would be critical tasks and weakly effective. Both these goals can be instead achieved by referring to suitable synchronous reference frames, as pointed out in the following subsections.

3.1 ft synchronous reference frame

The ft synchronous reference frame, which has been presented firstly in [25], makes T_e independent from ϑ_{pu}, thus enabling the design of effective current control loops that minimise torque ripple. The ft synchronous reference frame enables also a fair flux-weakening capability, as pointed out in [46]. The relationships between space vectors in the $\alpha\beta$ and ft reference frames are expressed in the following equation:

$$\begin{aligned} d_{ft} &= \delta\cdot d_{\alpha\beta} \\ d_{\alpha\beta} &= \gamma\cdot d_{ft} \end{aligned}, \quad d \in \{v, i, e\} \tag{13}$$

where

$$\delta = \frac{\sigma}{2}\left(-\sqrt{3}\left(1 - \vartheta_{\mathrm{pu}}\right) + j\left(1 + \vartheta_{\mathrm{pu}}\right)\right), \quad \delta\cdot\gamma = 1. \tag{14}$$

Therefore, by combining (13) with (5) and (9), voltage and torque equations become, respectively,

$$v_{ft} = \left(r + \omega_{\mathrm{pu}} L\xi_{ft}\right)i_{ft} + L\frac{\mathrm{d}i_{ft}}{\mathrm{d}t} + e_{ft} \tag{15}$$

$$T_e = 2p\Lambda\cdot i_t \tag{16}$$

in which ω_{pu} is the time derivative of ϑ_{pu} and it can be computed as

$$\omega_{\mathrm{pu}} = \frac{3}{\pi}p\omega_m = \frac{3}{\pi}p\omega\,. \tag{17}$$

Furthermore, ξ_{ft} and e_{ft} are expressed, respectively, as

$$\begin{aligned} \xi_{ft} &= \frac{1}{2}\frac{1}{1 - \vartheta_{\mathrm{pu}} + \vartheta_{\mathrm{pu}}^2}\left(\left(1 - 2\vartheta_{\mathrm{pu}}\right) + j\sqrt{3}\right) \\ e_{ft} &= j\frac{4}{3}E\left(1 - \vartheta_{\mathrm{pu}} + \vartheta_{\mathrm{pu}}^2\right). \end{aligned} \tag{18}$$

Hence, (16) reveals that the PMBDCM torque does not depend directly on ϑ_{pu} further and it is proportional to just the t current component; this is the most important advantage of moving into the ft reference frame, in which the torque can be held constant at (T_e^*) simply by driving i_t to the corresponding reference value (i_t^*). Whereas i_f^* can be held constant at zero in order to not increase Joule losses unsuitably; alternatively, i_f^* can be set in accordance with flux-weakening operation needs in order to extend CPSR properly. In this regard, it is worth noticing that this control strategy is the same widely employed for PMBACM, as pointed out in [46]; in particular, the Park transformation is generally

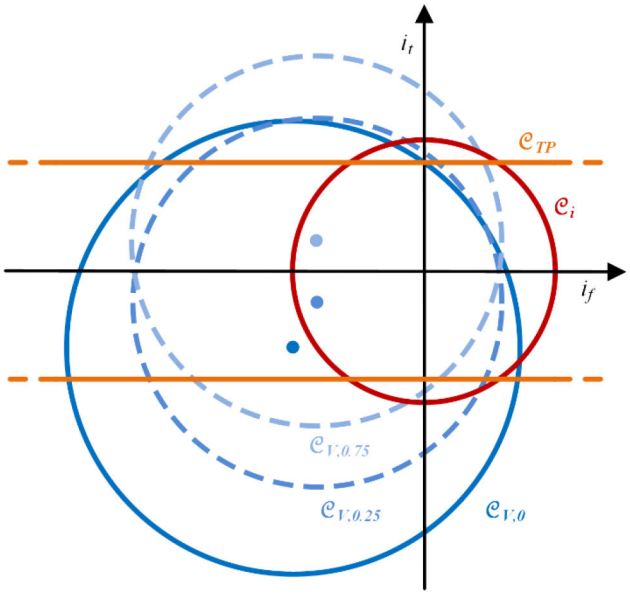

Fig. 2 *Equivalent current constraints of PMBDCM on the (i_f, i_t) plane, in which $\mathscr{C}_V$ is drawn for different ϑ_{pu} values (0, 0.25 and 0.75)*

applied to PMBACMs for moving from stationary to *dq* synchronous reference frame; as a result, T_e is driven by means of i_q only, while i_d can be injected suitably in accordance with flux-weakening operation needs.

In order to define the reference current profile in the *ft* synchronous reference frame, PMBDCM operating constraints must be considered and expressed in terms of equivalent current constraints. Therefore, by combining (13) with (10), torque and power limitations can be expressed as

$$|i_t^*| \le I_n \cdot \min\left\{1, \frac{\omega_{m,n}}{|\omega_m|}\right\}, \quad I_n = \frac{T_{e,n}}{2p\Lambda}. \tag{19}$$

Considering now current limitation, combining (13) with (11) and assuming i_{ft}^* constant at steady-state operation yields

$$\underline{|\gamma|}^2 |i_{ft}^*|^2 \le \frac{4}{3} \cdot \hat{I}^2, \quad \underline{|\gamma|}^2 = \frac{2}{3}\frac{\pi}{\sqrt{3}}. \tag{20}$$

Consequently, the following relationship holds:

$$|i_{ft}^*|^2 \le \hat{I}_{ft}^2, \quad \hat{I}_{ft}^2 = \frac{2\sqrt{3}}{\pi}\hat{I}^2. \tag{21}$$

Regarding voltage saturation, combining (13) with (12) leads to

$$|v_{ft}| \le |\delta| \frac{V_{DC}}{\sqrt{3}}. \tag{22}$$

Furthermore, by substituting (15) into (22) and still assuming to be at steady-state operation ($i_{ft} = i_{ft}^* = \text{const.}$), the corresponding equivalent current constraint is

$$|i_{ft}^* - \varsigma_{ft}| \le \rho_{ft} \tag{23}$$

in which

$$\varsigma_{ft} = -\frac{e_{ft}}{r + \omega_{pu} L \xi_{ft}}, \quad \rho_{ft} = \frac{|\delta|}{|r + \omega_{pu} L \xi_{ft}|} \frac{V_{DC}}{\sqrt{3}}. \tag{24}$$

All the equivalent current constraints just introduced can be drawn on the (i_f, i_t) plane, as shown in Fig. 2. Considering torque and power limitations at first ($\mathscr{C}_{TP}$), these define a plane region bounded by two straight lines, symmetrically displaced with respect to the i_f axis. These lines do not change when the rotor speed is lower than the rated value, as highlighted in (19); this means that torque limitation constrains i_t more than the power limitation at low speed operation, whereas the opposite occurs beyond the rated speed. Regarding the current limitation ($\mathscr{C}_i$), it consists of a circle of radius $\hat{I}_{ft}$ and centred in the origin at any PMBDCM operating condition. Different considerations go for voltage saturation ($\mathscr{C}_V$), whose shape and position depend on both rotor speed and ϑ_{pu} in accordance with (24) and (18). In particular, $\mathscr{C}_V$ consists of multiple circles, whose radius and centre vary significantly within each PMBDCM operating sector, even at constant rotor speed, as highlighted in Fig. 2. This introduces additional issues in PMBDCM control system design compared to PMBACM, for which $\mathscr{C}_V$ consists of a single circle for any rotor position value. Therefore, suitable assumptions and considerations are advisable in order to make $\mathscr{C}_V$ not dependent on ϑ_{pu}, as well as for enabling proper flux-weakening operation, as pointed out in Section 4.

3.2 φτ synchronous reference frame

One of the main drawbacks of the *ft* synchronous reference frame consists of a non-isometric transformation from the *αβ* stationary reference frame and vice versa. This means that magnitudes of *ft* voltage and current vectors are weighted by $|\delta|$, which varies with ϑ_{pu} in accordance with the following relationship:

$$|\delta| = \sqrt{1 - \vartheta_{pu} + \vartheta_{pu}^2}. \tag{25}$$

This does not represent a critical issue for managing current limitation constraint as far as average values are concerned, as pointed out in (20) and (21). However, voltage saturation constraint is affected noticeably by (25), as highlighted by (24); in particular, $\mathscr{C}_V$ radius varies significantly within each operating sector, together with $\mathscr{C}_V$ centre. Consequently, although torque and power management benefits from the *ft* synchronous reference frame, managing voltage saturation constraint effectively is still a difficult task in this synchronous reference frame, may resulting in weak PMBDCM flux-weakening capability.

Based on the previous considerations, a novel *φτ* synchronous reference frame, which is alternative to the *ft* synchronous reference frame, is presented in this study. It is still based on (13) but aims at preserving the magnitude of voltage and current space vectors suitably, leading to the following relationships:

$$\begin{aligned} d_{\varphi\tau} &= \tilde{\delta} \cdot d_{\alpha\beta} \\ d_{\alpha\beta} &= \tilde{\gamma} \cdot d_{\varphi\tau} \end{aligned}, \quad d \in \{v, i, e\} \tag{26}$$

where

$$\tilde{\delta} = \frac{\delta}{|\delta|}, \quad \tilde{\gamma} = \frac{\gamma}{|\gamma|} = |\delta| \cdot \gamma. \tag{27}$$

Consequently, by combining (26) with (5) and (9), voltage and torque equations in the *φτ* synchronous reference frame become

$$v_{\varphi\tau} = (r + \omega_{pu} L \xi_{\varphi\tau}) i_{\varphi\tau} + L \frac{\mathrm{d}i_{\varphi\tau}}{\mathrm{d}t} + e_{\varphi\tau} \tag{28}$$

$$T_e = 2p\Lambda \cdot i_\tau \cdot \sqrt{1 - \vartheta_{pu} + \vartheta_{pu}^2} \tag{29}$$

in which

$$\xi_{\varphi\tau} = j\frac{\sqrt{3}}{2}\frac{1}{1 - \vartheta_{pu} + \vartheta_{pu}^2}, \quad e_{\varphi\tau} = j\frac{4}{3}E\sqrt{1 - \vartheta_{pu} + \vartheta_{pu}^2}. \tag{30}$$

Focusing on voltage equation at first, the comparison between (28) and (15) highlights no detectable differences; these are revealed by comparing (30) to (18), namely $\xi_{\varphi\tau}$ presents just the imaginary component compared to ξ_{ft}, while the dependence of $e_{\varphi\tau}$ on ϑ_{pu} is

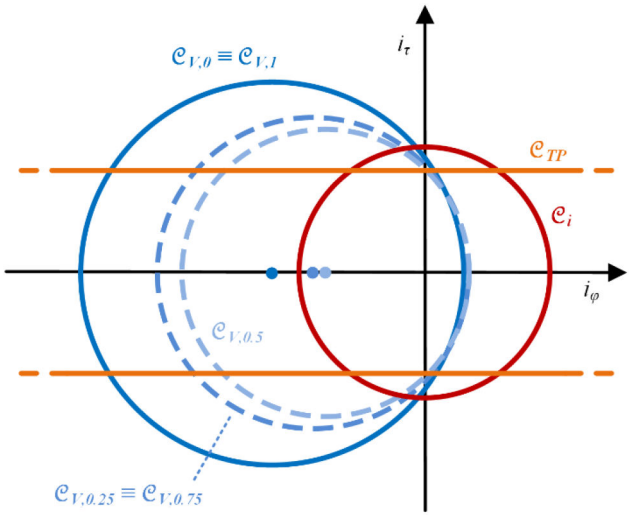

Fig. 3 *Equivalent current constraints of PMBDCM on the (i_φ, i_τ) plane, in which $\mathscr{C}_V$ is shown for different ϑ_{pu} values (0, 0.25, 0.5, and 0.75)*

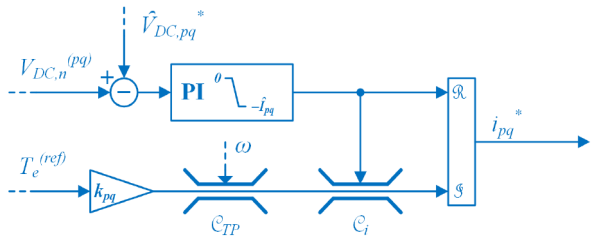

Fig. 4 *The reference currents control block, in which (pq) denotes (ft) or (φτ) alternatively and k_{pq} can be derived easily from either (16) or (31)*

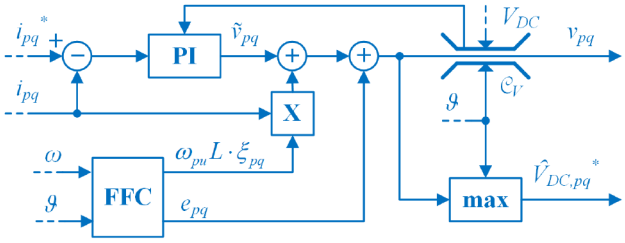

Fig. 5 *pq current loops control block, in which (pq) denotes (ft) or (φτ) alternatively and FFC means feed-forward compensation*

lightened by the square root operator compared to e_{ft}. Both these considerations suggest that the φτ synchronous reference frame may be more suitable than the ft synchronous reference frame in terms of voltage saturation management and, thus, flux-weakening capability. However, these potential benefits come at the cost of restoring the dependence of T_e on ϑ_{pu}, as easy detectable by comparing (29) to (16); this means that unsuitable torque ripple occurs at steady-state operation ($i_{\varphi\tau}$ = $i_{\varphi\tau}^{*}$ = const.), which is assessable in about 15% in accordance with the evolution of (25) within each PMBDCM operating sector. In addition, assuming i_τ constant, this torque ripple affects the average torque achievable in the $\varphi\tau$ synchronous reference frame in accordance with the following relationship:

$$\underline{T_e^{(\varphi\tau)}} = \int_0^1 T_e|_{i_\tau = \text{cnst.}} \mathrm{d}\vartheta_{\text{pu}} = 2p\Lambda \cdot i_\tau \cdot \psi_{\varphi\tau} \tag{31}$$

in which

$$\psi_{\varphi\tau} = \int_0^1 \sqrt{1 - \vartheta_{\text{pu}} + \vartheta_{\text{pu}}^2}\,\mathrm{d}\vartheta_{\text{pu}} = \frac{3}{8}\ln(3) + \frac{1}{2} \cong 0.912. \tag{32}$$

Therefore, in order to guarantee the same average torque in both the *ft* and the φτ synchronous reference frames, the reference τ current component should be computed as

$$i_\tau^{*} = \frac{i_t^{*}}{\psi_{\varphi\tau}}. \tag{33}$$

Based on all the previous considerations, it is possible to carry out the analysis of the PMBDCM operating constraints on the novel $\varphi\tau$ synchronous reference frame. In particular, by substituting (33) into (19), torque and power limitation constraints become

$$|i_\tau^{*}| \le I_n^{(\varphi\tau)} \cdot \min\left\{1, \frac{\omega_{m,n}}{|\omega_m|}\right\}, \quad I_n^{(\varphi\tau)} = \frac{I_n}{\psi_{\varphi\tau}}. \tag{34}$$

While current limitation constraint can be easily achieved from (11) due to the isometric transformation defined by (26), leading to

$$|i_{\varphi\tau}^{*}|^2 \le \frac{4}{3} \cdot \hat{I}^2. \tag{35}$$

The same goes also for voltage saturation constraint expressed by (12), which becomes

$$|v_{\varphi\tau}| \le \frac{V_{\text{DC}}}{\sqrt{3}}. \tag{36}$$

Therefore, substituting (28) into (36) and assuming to be at steady-state operation ($i_{\varphi\tau} = i_{\varphi\tau}^{*} = \text{const.}$), the equivalent current constraint is

$$|i_{\varphi\tau}^{*} - \varsigma_{\varphi\tau}| \le \rho_{\varphi\tau} \tag{37}$$

in which

$$\varsigma_{\varphi\tau} = -\frac{e_{\varphi\tau}}{r + \omega_{\text{pu}} L \xi_{\varphi\tau}}, \quad \rho_{\varphi\tau} = \frac{1}{|r + \omega_{\text{pu}} L \xi_{\varphi\tau}|} \frac{V_{\text{DC}}}{\sqrt{3}}. \tag{38}$$

The PMBDCM operating constraints on the (i_φ,i_τ) plane are depicted in Fig. 3. The comparison between this figure and Fig. 2 reveals the same shapes of all the constraints, as expected. However, although $\mathscr{C}_V$ still corresponds to multiple circles, these seem less variable with ϑ_{pu} in terms of both radius and centre. This is also proved by the fact that the same $\mathscr{C}_V$ is achieved at ϑ_{pu} and $1–\vartheta_{\text{pu}}$; as a result, much less area is 'swept' by $\mathscr{C}_V$ on the (i_φ, i_τ) plane when ϑ_{pu} varies within [0,1) compared to what occurring in the (i_f, i_t) plane. Therefore, the PMBDCM operating region on the (i_φ, i_τ) plane seems more regular than on the (i_f, i_t) plane, which results in a more effective PMBDCM voltage saturation management at high speed operation.

4 PMBDCM control system design

Based on (15) and (16) or, alternatively, on (28) and (31), it is possible to design a suitable FW-SVC for PMBDCM in the *ft* or $\varphi\tau$ synchronous reference frame. In particular, two main stages can be identified and carried out sequentially: the first stage consists of setting the most suitable reference current profile (i_{ft}^{*} or $i_{\varphi\tau}^{*}$) in accordance with PMBDCM operating constraints and torque demand ($T_e^{(ref)}$). Once the reference currents have been set, they must be tracked through proper current control loops, which represent the second stage of the control system. The two stages of FW-SVC are shown in Figs. 4 and 5 and detailed in the following subsections, together with the general overview of the proposed control scheme (Fig. 6).

4.1 Stage one: reference current setup

Denoting by *pq* the generic synchronous reference frame, in which *pq* corresponds to either *ft* or $\varphi\tau$ alternatively, the reference current

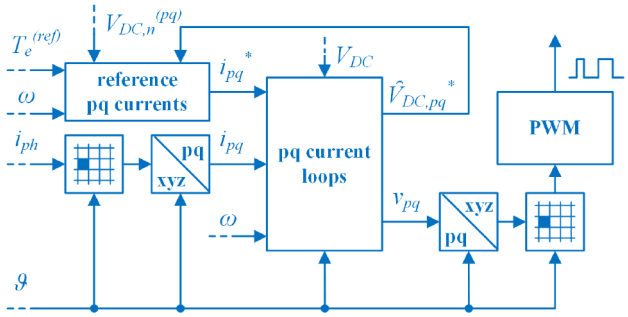

Fig. 6 *General overview of the proposed FW-SVCs, in which i_{ph} denotes the (i_u, i_v, i_w) current vector and (pq) denotes (ft) or ($\varphi\tau$) alternatively*

vector must be synthesised properly by considering the influence of each PMBDCM operating constraint on i_p^* and i_q^*, as highlighted in Fig. 4. In particular, voltage saturation constraint should affect only i_p^* directly, because the p current component exhibits inherent flux-weakening capability and it is not subjected to any torque or power constraint. Therefore, a voltage follower PI-based control loop can be designed so that appropriate flux-weakening operation can be assured at any operating condition [34]. However, this task requires coping with the dependence of the voltage saturation constraint on ϑ_{pu}, as pointed out and discussed briefly in the previous Section 3.

Hence, referring to the ft synchronous reference frame at first, the DC-link voltage required by PMBDCM at steady-state operation can be computed in accordance with (22) and (15) as

$$V_{\text{DC},ft}^* = \sqrt{3}|\gamma||v_{ft}^*|, \quad v_{ft}^* = (r + \omega_{\text{pu}} L \xi_{ft}) i_{ft}^* + e_{ft}. \tag{39}$$

However, even if i_{ft}^* and ω_m are constant, both ξ_{ft} and e_{ft} vary with ϑ_{pu}, as highlighted by (18). Consequently, $V_{\text{DC},ft}^*$ also varies with ϑ_{pu}, revealing itself as an unsuitable variable for i_f^* computation purposes. Nevertheless, since voltage saturation constraint must be satisfied at any operating condition, just the peak value of $V_{\text{DC},ft}^*$ within each operating sector can be considered for determining i_f^*; this value does not depend on ϑ_{pu} and can be determined in accordance with the following relationship:

$$\hat{V}_{\text{DC},ft}^* = \max_{0 \le \vartheta_{\text{pu}} < 1} \{V_{\text{DC},ft}^*\}. \tag{40}$$

As a result, the voltage follower PI regulator can process the error between the rated DC-link voltage ($V_{\text{DC},n}^{(ft)}$) and $\hat{V}_{\text{DC},ft}^*$ for synthesising i_f^*, as highlighted in Fig. 4. In this regard, $V_{\text{DC},n}^{(ft)}$ is a constant value that can be computed as

$$V_{\text{DC},n}^{(ft)} = \hat{V}_{\text{DC},ft}^* \Big|_{i_f^* = 0,\, i_t^* = I_n,\, \omega_m = \omega_{m,n}}. \tag{41}$$

Similar considerations go for the synthesis of the reference current profiles in the $\varphi\tau$ synchronous reference frame, although some differences occur. In particular, (39)–(41) are replaced by the following relationships:

$$V_{\text{DC},\varphi\tau}^* = \sqrt{3}|v_{\varphi\tau}^*|, \quad v_{\varphi\tau}^* = (r + \omega_{\text{pu}} L \xi_{\varphi\tau}) i_{\varphi\tau}^* + e_{\varphi\tau} \tag{42}$$

$$\hat{V}_{\text{DC},\varphi\tau}^* = \max_{0 \le \vartheta_{\text{pu}} < 1} \{V_{\text{DC},\varphi\tau}^*\} \tag{43}$$

$$V_{\text{DC},n}^{(\varphi\tau)} = \hat{V}_{\text{DC},\varphi\tau}^* \Big|_{i_\varphi^* = 0,\, i_\tau^* = I_n^{(\varphi\tau)},\, \omega_m = \omega_{m,n}}. \tag{44}$$

Hence, different maximum voltage demand and rated DC-link voltage are concerned in the ft and $\varphi\tau$ synchronous reference frames, which result in different flux-weakening capability.

Regardless of the specific synchronous reference frame, it is worth highlighting that i_p^* has to be determined not only in accordance with voltage saturation constraint, but also with the current limitation constraint. In this regard, although current limitation constrains i_p^* and i_q^* equally, the achievement of i_p^* should be always prioritised over i_q^* because it is preparatory for achieving proper PMBDCM performances at high speed operation. Once i_p^* has been computed, i_q^* can be determined based on $T_e^{(ref)}$ by complying with either (19) and (21) or (34) and (35) sequentially, as still highlighted in Fig. 4. In particular, since i_q^* depends on $T_e^{(ref)}$ primarily and i_p^* does not contribute to neither torque nor power delivered by PMBDCM, the torque and power limitation constraints affect only i_q^* directly.

In conclusion, it is worthy of note that the gains of the voltage follower PI regulator should be set carefully whatever the chosen synchronous reference frame is. This is because relatively high gain values may be desirable for achieving fast p current injection as soon as any DC-link voltage deficit is detected. However, voltage deficits do not always correspond to flux-weakening needs as they occur also during PMBDCM dynamic operations; in those cases, relatively low gain values should be desirable in order to prevent p current injections that increase Joule losses without bringing any benefit. Consequently, a suitable trade-off between flux-weakening capability and proper PMBDCM dynamic operation must be assured.

4.2 Stage two: current loops

The second stage of FW-SVC is devoted to ensure a proper reference current tracking; for this purpose, a PI-based control system can be employed, as shown in Fig. 5 and already pointed out in [25]. In particular, this control system can be designed based on the following auxiliary voltage vector:

$$\tilde{v}_{pq} = v_{pq} - (\omega_{\text{pu}} L \xi_{pq} \cdot i_{pq} + e_{pq}), \quad pq \in \{ft, \varphi\tau\}. \tag{45}$$

The combination of (45) with either (15) or (28) yields

$$\tilde{v}_{pq} = r i_{pq} + L \frac{\text{d}i_{pq}}{\text{d}t}, \quad pq \in \{ft, \varphi\tau\}. \tag{46}$$

As a result, both PI regulators can be designed based on (46) in order to achieve the desired current dynamic performances.

Once $\tilde{v}_{pq}$ has been determined, v_{pq} can be computed in accordance with (45) and it can be made compliant with the voltage saturation constraint. Furthermore, the unsaturated voltage vector concurs to determine $\hat{V}_{\text{DC},pq}^*$ in accordance with either (39) or (42). Among all the $V_{\text{DC},pq}^*$ values collected within each operating sector, the maximum one represents $\hat{V}_{\text{DC},pq}^*$ in accordance with either (40) or (43); this value is updated periodically and feed back to the reference currents block because it is necessary for determining i_p^*, as pointed out in the previous subsection.

4.3 Control system general overview

The general overview of the proposed FW-SVC is shown in Fig. 6. In particular, $\{i_u, i_v, i_w\}$ is converted into the corresponding $\{x, y, z\}$ and, then, into pq current components; meanwhile, reference current components can be determined based on the chosen control strategy, which may address flux-weakening operation issue. Once the reference currents have been set and the corresponding actual current values have been available, current tracking can be assured by two control loops with the aim of synthesising the most suitable voltage space vector. This is then converted from the pq synchronous to the $\{u, v, w\}$ reference frame and, in turn, into the most suitable PWM pattern for driving the DC/AC converter that supplies the PMBDCM.

In conclusion, it is worth highlighting that the proposed PMBDCM control structure is very similar to that usually employed for PMBACM. However, in spite of many similarities, the synthesis of the reference current profile in the generic pq synchronous reference frame and the design of the corresponding

current control loops require additional assumptions for PMBDCM compared to PMBACM; this is due to the non-linearities of (15) and, to a less extent, of (28), which suggest employing either (40) or (43) instead of the actual magnitude of the voltage vector, as usually occurs for PMBACM.

5 Simulations

5.1 Simulation setup

A simulation study has been carried out in the MATLAB–Simulink environment at the aim of assessing the effectiveness of the proposed FW-SVC designed on the novel $\varphi\tau$ synchronous reference frame. Therefore, reference is made to the high-speed PMBDCM presented in [47], which requires a very wide CPSR and, thus, represents an ideal case study for testing flux-weakening capability of the proposed control system. An overview of the overall simulation setup is shown in Fig. 7; the PMBDCM, whose main parameters are resumed in Table 2, is supplied by an energy storage system through a three-phase DC/AC converter. Due to the very high target maximum speed of the PMBDCM (100 krpm), the converter switching frequency has been set at about 80 kHz. Furthermore, the rated voltage of the energy storage system has been set at 720 V; this value is fairly greater than $V_{DC,n}^{(ft)}$ (about 640 V) in order to ensure some voltage reserve for PMBDCM dynamic operation only. However, it is worth noting that $V_{DC,n}^{(\varphi\tau)}$ (about 540 V) is much lower than $V_{DC,n}^{(ft)}$, revealing the benefit of using the $\varphi\tau$ synchronous reference frame in terms of PMBDCM voltage management, but at the cost of increased torque ripple.

Simulation study regards three different versions of PMBDCM space vector control for comparison purposes: the SVC proposed in [25], the SVC designed into the *ft* synchronous reference frame (FW-SVC-ft) [46] and the SVC designed into the $\varphi\tau$ synchronous reference frame proposed in this study (FW-SVC-φτ). All these control systems share the same control structure, namely that shown in Fig. 6 and described in detail in the previous section. However, SVC holds the reference f current component constant at zero at any operating condition; this does not occur with either FW-SVC-ft or FW-SVC-φτ, which share the same control structure but differ for the specific functions implemented. Conventional current commutation control, which has been used as a benchmark in both [25, 46], is not considered in this study due to its weak performances, especially at high speed operation.

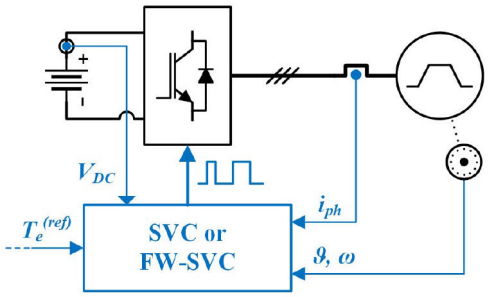

Fig. 7 *Simulation setup: a three-phase PMBDCM supplied by an energy storage system through a DC/AC converter, which is driven by SVC or FW-SVC alternatively*

All the control algorithms considered for simulation share the same current dynamic performances, namely the bandwidth of each current PI regulator has been set at 20 kHz. Similarly, the sampling time interval has been chosen always equal to 12.8 µs. It is assumed also that relatively high-resolution values of both ϑ and ω are available; these could be provided either by a high-resolution position sensor or by resorting to an appropriate sensorless algorithm.

Simulations refer to a PMBDCM start up at first, in correspondence of which the reference torque is set at $T_{e,n}$; while the load torque has been set so that a steady-state speed value equal to the rated one should be reached. Subsequently, at 0.1 s, the load torque is suddenly decreased in order to achieve a higher steady-state speed value (1.5 times $\omega_{m,n}$). The load torque is decreased again at 0.2 s in order to enable the achievement of a steady-state speed value of 3 times $\omega_{m,n}$, which is very close to the PMBDCM maximum speed. As a result, the performances achievable by SVC, FW-SVC-ft and FW-SVC-φτ can be assessed at different operating conditions, by highlighting their most important strengths and weaknesses.

5.2 Simulation results

Simulation results are summarised in Figs 8-9; all of them are shown in per unit, namely each quantity has been normalised by means of the corresponding base value shown in Table 3. Considering PMBDCM start-up, it can be seen that SVC and FW-SVC-ft perform in the same way because no *f* current component is needed below the rated speed. Therefore, *t* current component is driven in accordance with the reference torque demand, while i_f is held constant at zero. Worse performances in terms of torque ripple are achieved by FW-SVC-φτ, as expected and well highlighted in Fig. 8. However, Fig. 9 reveals that PMBDCM voltage demand is significantly reduced by FW-SVC-φτ compared to the other two control schemes (from 1.0 to 0.8 pu), while current demand is almost the same in all cases.

This means that FW-SVC-φτ is the most suitable control algorithm in terms of PMBDCM voltage saving, as foreseen during the design stage.

Considering now the evolutions achieved after the first load drop (0.1–0.2 s), constant-power operation is somehow assured in all cases, but some differences occur. First of all, PMBDCM voltage demand achieved by SVC increases unsuitably, far beyond the DC-link voltage due to the lack of any flux-weakening capability (Fig. 9). As a result, torque ripple occurs (Fig. 8), which, however, does not prevent the achievement of the target speed (1.5 pu), as well as PMBDCM constant-power operation. Furthermore, i_f and i_φ are held constant at zero almost successfully, as shown in Figs. 10 and 11; this enables PMBDCM current demand to decrease properly in accordance with PMBDCM constant-power operation, as shown in Fig. 9.

However, these performances come at the cost of using the DC-link voltage reserve at steady-state operation, which should be instead employed during dynamic operation only.

Still referring to the first load drop, enhanced performances are achieved by FW-SVC-ft compared to SVC, as expected. In particular, as soon as the speed overcomes the rated value, an increasing DC-link voltage deficit is detected, thus a corresponding negative f current component is injected. Consequently, PMBDCM

Table 2 High-speed PMBDCM parameter and rated values

	r	L	p	Λ	$T_{e,n}$	$\omega_{m,n}$
value	11	546	1	0.0589	12.7	30
unit	mΩ	µH	—	Vs	Nm	krpm

Table 3 Simulation base values

	$T_{e,b}$	$\omega_{m,b}$	$P_{m,b}$	I_b	V_b
value	12.7	30	39.9	107.83	639.86
unit	Nm	krpm	kW	A	V

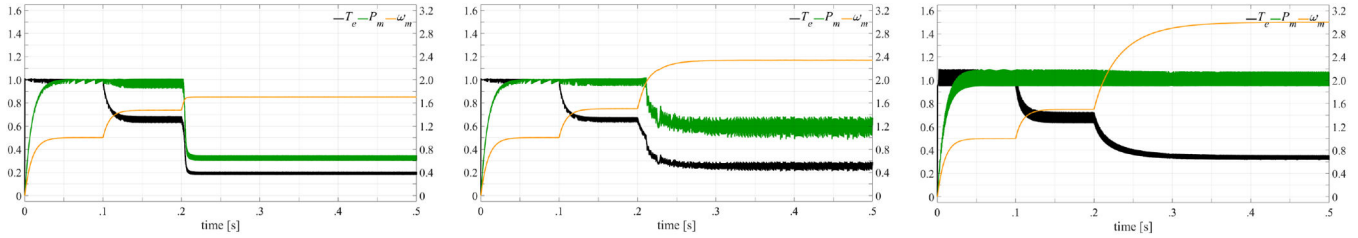

Fig. 8 *Evolutions of torque (black), power (green) and speed (orange) achieved by SVC (on the left), FW-SVC-ft (in the middle) and FW-SVC-φτ (on the right): y-axis of torque and power is on the left, while y-axis of speed is on the right*

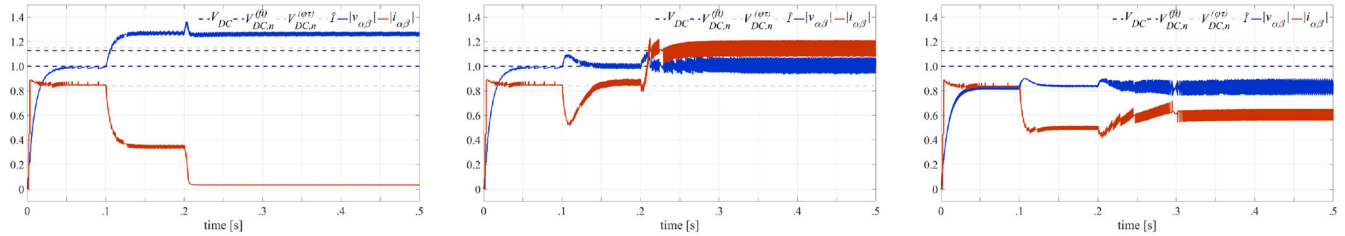

Fig. 9 *Voltage (blue) and current (red) demand achieved by SVC (on the left), FW-SVC-ft (in the middle) and FW-SVC-φτ (on the right), together with V_{DC} (black), $V_{DC,n}^{(ft)}$ (blue), $V_{DC,n}^{(\varphi\tau)}$ (light blue) and $\hat{I}$ (pink) thresholds*

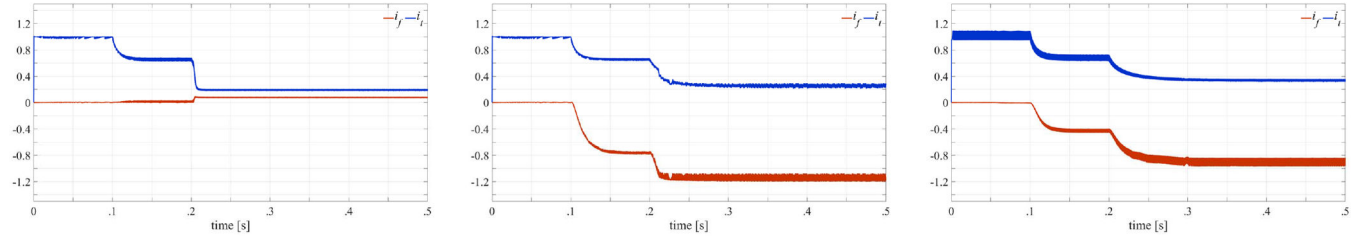

Fig. 10 *i_f (red) and i_t (blue) achieved by SVC (on the left), FW-SVC-ft (in the middle) and FW-SVC-φτ (on the right)*

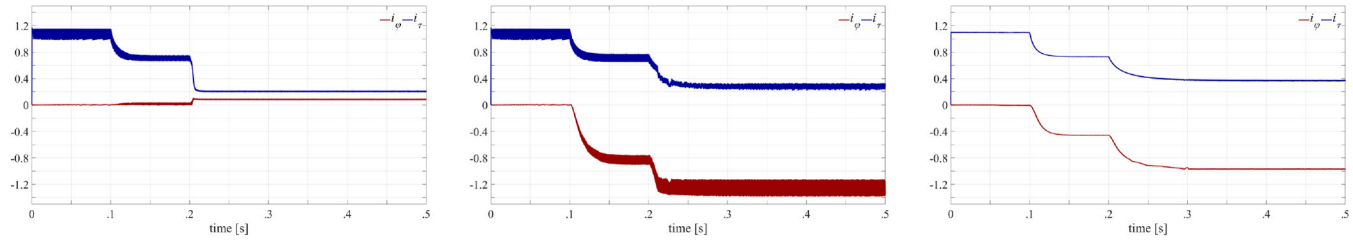

Fig. 11 *i_φ (red) and i_τ (blue) achieved by SVC (on the left), FW-SVC-ft (in the middle) and FW-SVC-φτ (on the right)*

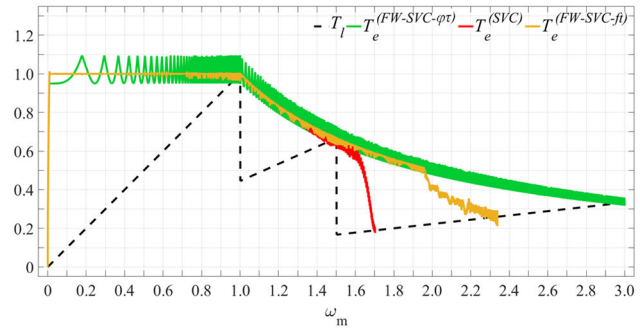

Fig. 12 *Torque–speed evolutions achieved by SVC (red), FW-SVC-ft (orange) and FW-SVC-φτ (green), together with the PMBDCM load torque (dashed black)*

voltage demand increases at first due to the delayed response of the voltage follower PI regulator, but it is soon restored at the corresponding rated value as shown in Fig. 9. The latter reveals also that PMBDCM current demand decreases and then increases, by reaching a steady-state value slightly greater than the rated one; this is because the reduction of i_t due to constant-power operation is less and, then, more than compensated by the i_f injection. Such negative i_f values enable FW-SVC-ft to keep PMBDCM voltage demand within V_{DC}, which does not occur by SVC. As a result, torque ripple is minimised to the maximum extent because the frequent drops of i_t occurring with SVC due to the significant DC-link voltage deficit are avoided at the cost of slightly increasing PMBDCM current demand. Furthermore, FW-SVC-ft preserves DC-link voltage reserve properly.

Still focusing on the first load drop, FW-SVC-φτ achieves worse performances than SVC and, especially, than FW-SVC-ft in terms of torque ripple (Fig. 8), but much better performances in terms of both voltage and current demands (Fig. 9). In particular, voltage demand is kept at about 80% of that required by FW-SVC-ft; this is possible by injecting an appropriate φ current component, as shown in Fig. 11. In this regard, it is worth noting that, differently from FW-SVC-ft, the reduction of i_τ due to constant-power operation is always less than compensated by the i_φ injection required by FW-SVC-φτ; this leads to a much lower current demand and, thus, increased efficiency achieved by FW-SVC-φτ. However, this efficiency is still worse than that achievable by SVC, which does not account for any f or φ current component but at the cost of using DC-link voltage reserve unsuitably.

At 0.2 s a further load drop is imposed in order to force the PMBDCM to achieve a very high steady-state speed value (3.0 pu).

Table 4 Key performance indexes

	SVC	FW-SVC-ft	FW-SVC-φτ
CPSR	1.60	1.95	> 3.0
$\hat{\omega}_m$	1.70	2.34	3.0
P_m @ $\hat{\omega}_m$	0.32	0.61	1.00

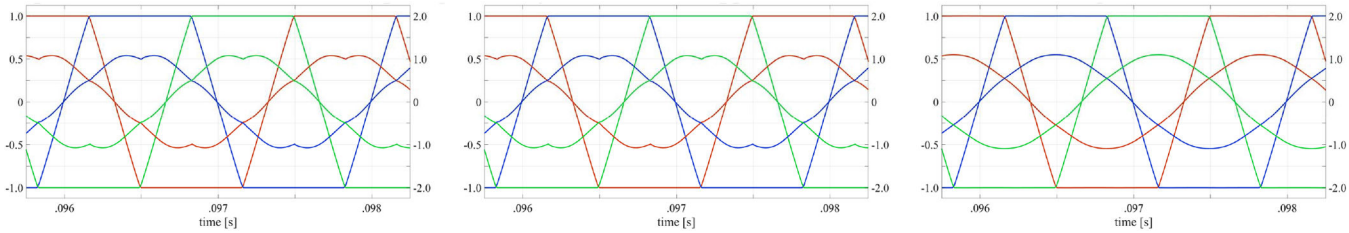

Fig. 13 *Back-emf (y-axis on the left) and current (y-axis on the right) evolutions achieved at the rated speed by SVC (on the left), FW-SVC-ft (in the middle) and FW-SVC-φτ (on the right): phase u (red), phase v (blue) and phase w (green)*

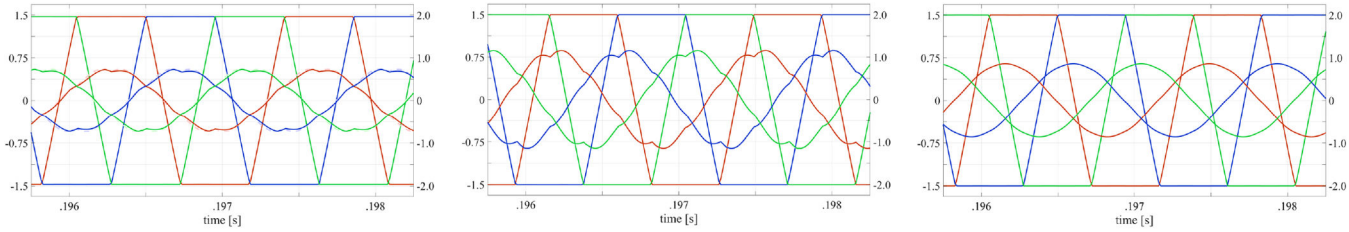

Fig. 14 *Back-emf (y-axis on the left) and current (y-axis on the right) evolutions achieved at ω_m = 1.5 pu by SVC (on the left), FW-SVC-ft (in the middle) and FW-SVC-φτ (on the right): phase u (red), phase v (blue) and phase w (green)*

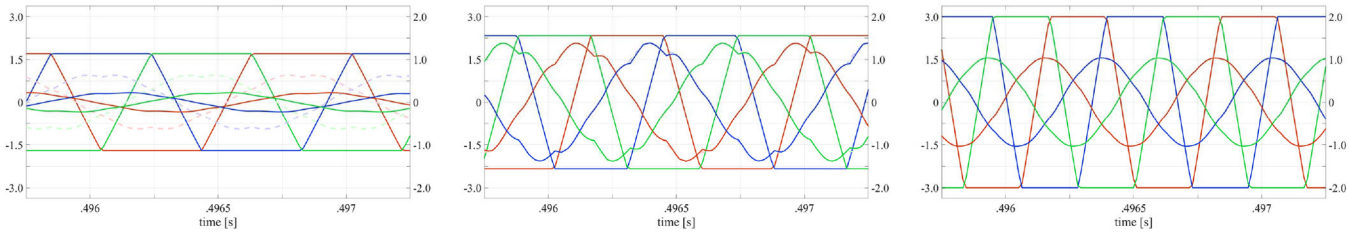

Fig. 15 *Back-emf (y-axis on the left) and current (y-axis on the right) evolutions achieved at maximum speed by SVC (on the left), FW-SVC-ft (in the middle) and FW-SVC-φτ (on the right): phase u (red), phase v (blue) and phase w (green)*

However, only FW-SVC-φτ is able to drive the PMBDCM successfully to this target, whereas both SVC and FW-SVC-ft highlight inherent limitations in terms of CPSR and maximum speed, as shown in Fig. 12 and Table 4.

In particular, SVC guarantees a CPSR of about 1.6 pu, beyond which reduced power operation occurs due to the excessive PMBDCM voltage demand. Consequently, torque and current demand drop significantly and a maximum speed of about 1.7 pu is achieved. Furthermore, small but positive f and φ current components arise, which are totally unsuitable in terms of both Joule losses and flux-weakening operation purposes.

Better performances are achieved by FW-SVC-ft, namely CPSR is extended from 1.6 pu to about 1.95 pu; however, beyond this speed value, f current component cannot decrease further due to current limitation constraint, as highlighted in Fig. 9. Consequently, reduced power operation occurs, over which a maximum speed of 2.34 pu is achieved. Much improved performance is obtained by FW-SVC-φτ, which is able to assure constant-power operation up to the target speed value, as well highlighted in both Figs. 8 and 12 and summed up in Table 4. Such enhanced capabilities are due to the relatively low current demand required by φ current component injection, especially if compared to FW-SVC-ft. Furthermore, the PMBDCM voltage demand is still kept at about 0.8 pu; this means that FW-SVC-φτ enables both voltage and current saving compared to FW-SVC-ft, resulting in extended CPSR and increased efficiency at the cost of higher torque ripple. Furthermore, the DC-link voltage could be decreased from 720 to 600 V safely because no effect would be determined on FW-SVC-φτ steady-state performances.

In conclusion, reference is made to steady-state back-emf and current evolutions achieved by SVC, FW-SVC-ft and FW-SVC-φτ at about 0.1, 0.2 and 0.5 s, which are shown in Figs. 13–15.

Focusing on Fig. 13 at first, SVC and FW-SVC-ft share the same current shapes, as expected because no f current component is needed yet. Furthermore, current evolutions are aligned with the corresponding back-emfs in order to maximise PMBDCM torque per unit current. The same goes also for FW-SVC-φτ, which, however, is characterised by almost sinusoidal currents, leading to some torque ripple. As the speed increases up to 1.5 pu, SVC current shapes do not change significantly, but their magnitude decreases in accordance with a lower PMBDCM torque demand, as highlighted in Fig. 14. Whereas significant distortions occur on the current profile achieved by FW-SVC-ft due to negative f current injection; this also introduces some angular displacement between current and back-emf waveforms. A similar angular displacement also occurs by means of FW-SVC-φτ, whose current shapes, however, are characterised by much less distortions than in the case of FW-SVC-ft. Considering now the steady-state current evolutions depicted in Fig. 15, it is worth pointing out that they refer to different speed and power values in accordance with the inherent limitations of each control algorithm. In particular, current shapes achieved by SVC at ω_m = 1.70 pu are somehow distorted, but still aligned with the back-emfs. However, they are quite far from the corresponding reference values (dashed lines depicted in Fig. 15) because SVC current tracking capability is prevented significantly

by the very high voltage demand occurring with this kind of control approach. Better results are achieved by FW-SVC-ft at $\omega_m = 2.34$ pu, namely current shapes are not so much distorted, but they are further displaced with respect to the back-emf waveforms. Furthermore, current magnitude is quite relevant due to the achievement of the current limitation constraint, meaning that the corresponding Joule losses are at the maximum allowable value. The best performances in terms of current shapes are surely achieved by FW-SVC-φτ, which is able to preserve current shapes and magnitude almost unchanged, even at a very high rotor speed (3.0 pu); while angular displacement between current and back-emf waveforms slightly increases due to a further decrease of i_φ. The results achieved by FW-SVC-φτ confirm that almost sinusoidal currents are advisable at high-speed operation, even for a PMBDCM, as pointed out in [48].

6 Conclusion

Two FW-SVCs algorithms for PMBDCMs have been presented and discussed extensively in this study. These FW-SVCs have been designed with reference to two different synchronous reference frames (*ft* and *φτ*) and enable complementary advantages and drawbacks. In particular, FW-SVC-ft assures minimum torque ripple and, thus, high reference torque tracking capability, but suffers from limited CPSR and maximum speed. Both these weaknesses are overcome by the FW-SVC-φτ proposed in this study, which is able to achieve very high CPSR and maximum speed at the cost of increased torque ripple, especially at low speed operation. However, this disadvantage is more than compensated by reduced voltage and current demands: the former results in lower voltage required at the DC link (–20%), while the latter results in improved energy efficiency at high speed operation. Further improvements on FW-SVC-φτ may be introduced, such as an appropriate prediction of the change of sectors in order to mitigate torque ripple and a 'hybridisation' with FW-SVC-ft, especially at low speed operation.

7 References

[1] Krishnan, R.: '*Permanent magnet synchronous and brushless DC motor drives*' (CRC Press, New York, 2010)

[2] Dorrell, D.G., Hsieh, M., Popescu, M., *et al.*: 'A review of the design issues and techniques for radial-flux brushless surface and internal rare-earth permanent-magnet motors', *IEEE Trans. Ind. Electron.*, 2011, **58**, (9), pp. 3741–3757

[3] Serpi, A., Fois, G., Deiana, F., *et al.*: 'Performance improvement of brushless DC machine by zero-sequence current injection'. Proc. of 41st Annual Conf. of the IEEE Industrial Electronics Society (IECON 2015), Yokohama (Japan), 2015, pp. 3804–3809

[4] Chan, T.F., Lai, L.L.: 'Permanent-magnet machines for distributed power generation: a review'. Proc. of IEEE Power Engineering Society General Meeting (PESGM 2007), Tampa (USA), 2007, pp. 1–6

[5] Chau, K.T., Chan, C.C., Liu, C.: 'Overview of permanent-magnet brushless drives for electric and hybrid electric vehicles', *IEEE Trans. Ind. Electron.*, 2008, **55**, (6), pp. 2246–2257

[6] Ani, S.O., Bang, D., Polinder, H., *et al.*: 'Human powered axial flux permanent magnet machines: review and comparison'. Proc. of 2nd IEEE Energy Conversion Congress and Exposition (ECCE 2010), Atlanta (GA, USA), 2010, pp. 4165–4170

[7] El-Refaie, A.M.: 'Motors/generators for traction/propulsion applications: a review', *IEEE Veh. Technol. Mag.*, 2013, **8**, (1), pp. 90–99

[8] Usman, A., Joshi, B.M., Rajpurohit, B.S.: 'A review of modeling, analysis and control methods of brushless DC motors'. 2016 Int. Conf. on Computation of Power, Energy Information and Communication (ICCPEIC), Chennai (India), 2016, pp. 337–343

[9] Lee, H.-W., Kim, T.-H., Ehsani, M.: 'Practical control for improving power density and efficiency of the BLDC generator', *IEEE Trans. Power Electron.*, 2005, **20**, (1), pp. 192–199

[10] Gatto, G., Marongiu, I., Perfetto, A., *et al.*: 'Three-phase operation of brushless DC motor drive controlled by a predictive algorithm'. Proc. of 32nd Annual Conf. on IEEE Industrial Electronics (IECON 2006), Paris (France), 2006, pp. 1166–1170

[11] Catuogno, G.R., Forchetti, D.G., Leidhold, R., *et al.*: 'Power flow maximization in permanent-magnet generators', *IEEE Trans. Ind. Electron.*, 2014, **61**, (12), pp. 6566–6573

[12] Patel, H.V., Chandwani, H.: 'Review paper on torque ripple mitigation techniques for PMBLDC motor'. 2017 Int. Conf. on Current Trends in Computer, Electrical, Electronics and Communication (CTCEEC), Mysore (India), 2017, pp. 669–674

[13] Shirvani Boroujeni, M., Markadeh, G.R.A., Soltani, J.: 'Torque ripple reduction of brushless DC motor based on adaptive input–output feedback linearization', *ISA Trans.*, 2017, **70**, pp. 502–511

[14] de Castro, A.G., Pereira, W.C.A., de Almeida, T.E.P., *et al.*: 'Improved finite control-set model-based direct power control of BLDC motor with reduced torque ripple', *IEEE Trans. Ind. Appl.*, 2018, **54**, (5), pp. 4476–4484

[15] Jiang, W., Liao, Y., Wang, J., *et al.*: 'Improved control of BLDCM considering commutation torque ripple and commutation time in full speed range', *IEEE Trans. Power Electron.*, 2018, **33**, (5), pp. 4249–4260

[16] Li, X., Jiang, G., Chen, W., *et al.*: 'Commutation torque ripple suppression strategy of brushless DC motor considering back electromotive force variation', *Energies*, 2019, **12**, (10), p. 1932

[17] Ustun, O., Kivanc, O.C., Senol, S., *et al.*: 'On field weakening performance of a brushless direct current motor with higher winding inductance: why does design matter?', *Energies*, 2018, **11**, (11), p. 3119

[18] Tan, B., Wang, X., Zhao, D., *et al.*: 'A lag angle compensation strategy of phase current for high-speed BLDC motors', *IEEE Access*, 2019, **7**, pp. 9566–9574

[19] Jiang, G., Xia, C., Chen, W., *et al.*: 'Commutation torque ripple suppression strategy for brushless DC motors with a novel noninductive boost front end', *IEEE Trans. Power Electron.*, 2018, **33**, (5), pp. 4274–4284

[20] Cao, Y., Shi, T., Li, X., *et al.*: 'A commutation torque ripple suppression strategy for brushless DC motor based on diode-assisted buck–boost inverter', *IEEE Trans. Power Electron.*, 2019, **34**, (6), pp. 5594–5605

[21] Liu, H., Zhang, H.: 'A novel direct torque control method for brushless DC motors based on duty ratio control', *J. Frankl. Inst.*, 2017, **354**, (10), pp. 4055–4072

[22] Mars, R., Bouzidi, B., Badsi, B.E., *et al.*: 'DTC of three-level inverter fed brushless DC motor drives with torque ripple reduction'. 2018 Thirteenth Int. Conf. on Ecological Vehicles and Renewable Energies (EVER), Monte-Carlo (Monaco), 2018, pp. 1–10

[23] Hao, L., Toliyat, H.A.: 'BLDC motor full speed range operation including the flux-weakening region'. 38th IAS Annual Meeting on Conf. Record of the Industry Applications Conf., 2003., Salt Lake City (UT, USA), 2003, vol. 1, pp. 618–624

[24] Ta, C.: 'Pseudo-vector control - An alternative approach for brushless DC motor drives'. 2011 IEEE Int. Electric Machines Drives Conf. (IEMDC), Niagara Falls (ON, Canada), 2011, pp. 1534–1539

[25] Serpi, A., Fois, G., Porru, M., *et al.*: 'Space vector control of permanent magnet brushless DC machines'. Proc. of 22nd Int. Conf. on Electrical Machines (ICEM 2016), Lausanne (Switzerland), 2016, pp. 1194–1200

[26] Yao, X., Lu, G., Zhao, J., *et al.*: 'Torque ripple minimization in brushless DC motor with optimal current vector control technique'. 2018 Chinese Automation Congress (CAC), Xi'an (China), 2018, pp. 2524–2529

[27] Chen, J., Li, M., Liu, J.: 'A new SVPWM-based control scheme of permanent magnetic brushless DC machine with trapezoidal back EMF waveforms'. 2018 33rd Youth Academic Annual Conf. of Chinese Association of Automation (YAC), Nanjing (China), 2018, pp. 1147–1151

[28] Khazaee, A., Zarchi, H.A., Markadeh, G.R.A.: 'Real-time Maximum torque per ampere control of brushless DC motor drive with Minimum torque ripple', *IEEE Trans. Power Electron.*, 2019, pp. 1–1

[29] Khazaee, A., Abootorabi Zarchi, H., Arab Markadeh, G.: 'Loss model based efficiency optimized control of brushless DC motor drive', *ISA Trans.*, 2019, **86**, pp. 238–248

[30] Li, Z., Wang, J., Zhou, L., *et al.*: 'Enhanced generalized vector control strategy for torque ripple mitigation of IPM-type brushless DC motors', *IEEE Trans. Power Electron.*, 2019, pp. 1–1

[31] Menis, R., Mezzarobba, M., Tessarolo, A.: 'A survey of mechanical and electromagnetic design techniques for permanent-magnet motor flux-weakening enhancement'. Proc. of Electrical Systems for Aircraft Railway and Ship Propulsion Conf. (ESARS 2012), Bologna (Italy), 2012, pp. 1–6

[32] Lu, D., Kar, N.C.: 'A review of flux-weakening control in permanent magnet synchronous machines'. Proc. of IEEE Vehicle Power and Propulsion Conf. (VPPC 2010), Lille (France), 2010, pp. 1–6

[33] Bolognani, S., Calligaro, S., Petrella, R., *et al.*: 'Flux-weakening in IPM motor drives: comparison of state-of-art algorithms and a novel proposal for controller design'. Proc. of the 2011 14th European Conf. on Power Electronics and Applications, Birmingham (UK), 2011, pp. 1–11

[34] Maric, D.S., Hiti, S., Stancu, C.C., *et al.*: 'Two flux weakening schemes for surface-mounted permanent-magnet synchronous drives. Design and transient response considerations'. Proc. of IEEE Int. Symp. on Industrial Electronics (ISIE 1999), Bled (Slovenia), 1999, vol. 2, pp. 673–678

[35] Liu, H., Zhu, Z.Q., Mohamed, E., *et al.*: 'Flux-weakening control of nonsalient pole PMSM having large winding inductance, accounting for resistive voltage drop and inverter nonlinearities', *IEEE Trans. Power Electron.*, 2012, **27**, (2), pp. 942–952

[36] Lin, P., Lai, Y.: 'Voltage control technique for the extension of DC-link voltage utilization of finite-speed SPMSM drives', *IEEE Trans. Ind. Electron.*, 2012, **59**, (9), pp. 3392–3402

[37] Kwon, T., Sul, S.: 'Novel antiwindup of a current regulator of a surface-mounted permanent-magnet motor for flux-weakening control', *IEEE Trans. Ind. Appl.*, 2006, **42**, (5), pp. 1293–1300

[38] Kwon, Y., Kim, S., Sul, S.: 'Voltage feedback current control scheme for improved transient performance of permanent magnet synchronous machine drives', *IEEE Trans. Ind. Electron.*, 2012, **59**, (9), pp. 3373–3382

[39] Inoue, Y., Morimoto, S., Sanada, M.: 'Control method suitable for direct-torque-control-based motor drive system satisfying voltage and current limitations', *IEEE Trans. Ind. Appl.*, 2012, **48**, (3), pp. 970–976

[40] Pellegrino, G., Armando, E., Guglielmi, P.: 'Direct-flux vector control of IPM motor drives in the Maximum torque per voltage speed range', *IEEE Trans. Ind. Electron.*, 2012, **59**, (10), pp. 3780–3788

[41] Inoue, Y., Morimoto, S., Sanada, M.: 'Comparative study of PMSM drive systems based on current control and direct torque control in flux-weakening control region'. Proc. of IEEE Int. Electric Machines Drives Conf. (IEMDC 2011), Niagara Falls (ON, Canada), 2011, pp. 1094–1099

[42] Václavek, P., Blaha, P.: 'Field weakening in PMSM model based predictive control'. Proc. of IEEE Vehicle Power and Propulsion Conf. (VPPC 2010), Kuala Lumpur (Malaysia), 2010, pp. 330–335
[43] Choi, C., Seok, J., Lorenz, R.D.: 'Deadbeat-direct torque and flux control for interior PM synchronous motors operating at voltage and current limits'. Proc. of 3rd IEEE Energy Conversion Congress and Exposition (ECCE 2011), Phoenix (Arizona), 2011, pp. 371–376
[44] Nalepa, R., Orlowska-Kowalska, T.: 'Optimum trajectory control of the current vector of a nonsalient-pole PMSM in the field-weakening region', *IEEE Trans. Ind. Electron.*, 2012, **59**, (7), pp. 2867–2876
[45] Bolognani, S., Bolognani, S., Peretti, L.*, et al.*: 'Combined speed and current model predictive control with inherent field-weakening features for PMSM drives'. Proc. of 14th IEEE Mediterranean Electrotechnical Conf. (MELECON 2008), Ajaccio (France), 2008, pp. 472–478
[46] Serpi, A., Fois, G., Porru, M.*, et al.*: 'Flux-weakening space vector control algorithm for permanent magnet brushless DC machines'. Proc. of IEEE Vehicle Power and Propulsion Conf. (VPPC 2018), Chicago (IL, USA), 2018, pp. 1–6
[47] Damiano, A., Floris, A., Fois, G.*, et al.*: 'Design of a high-speed ferrite-based brushless DC machine for electric vehicles', *IEEE Trans. Ind. Appl.*, 2017, **53**, (5), pp. 4279–4287
[48] Zhu, Z.Q., Shen, J.X., Howe, D.: 'Flux-weakening characteristics of trapezoidal back-EMF machines in brushless DC and AC modes'. 2006 CES/IEEE 5th Int. Power Electronics and Motion Control Conf., Shanghai (China), 2006, vol. 2, pp. 1–5